

Prediction of $I_g,6d_{3/2} \rightarrow I_g,7p_{1/2}$, $I_g,7s_{1/2} \rightarrow I_g,7p_{1/2}$ and $I_g,7p_{1/2} \rightarrow I_m,7s_{1/2}$ transition frequencies in $^{229}Th^{3+}$ ion

Shi-Cheng Yu(余师成), Cheng-Bin Li(李承斌), and Lei She(佘磊)
Citation: Chin. Phys. B, 2026, 35 (**2**): 023701. DOI: 10.1088/1674-1056/ae0016
http://cpb.iphy.ac.cn; http://iopscience.iop.org/cpb

What follows is a list of articles you may be interested in

Simulation and experiment of the cooling effect of trapped ion by pulsed laser

Chang-Da-Ren Fang(方长达人), Yao Huang(黄垚), Hua Guan(管桦), Yuan Qian(钱源), and Ke-Lin Gao(高克林)
Chin. Phys. B, 2021, 30 (**7**): 073701. DOI: 10.1088/1674-1056/abf91f

Direct loading of atoms from a macroscopic quadrupole magnetic trap into a microchip trap

Jun Cheng(程俊), Jing-fang Zhang(张敬芳), Xin-ping Xu(许忻平), Hai-chao Zhang(张海潮), Yu-zhu Wang(王育竹)
Chin. Phys. B, 2017, 26 (**3**): 033701. DOI: 10.1088/1674-1056/26/3/033701

Theoretical derivation and simulation of a versatileelectrostatic trap for cold polar molecules

Shengqiang Li(李胜强)
Chin. Phys. B, 2016, 25 (**11**): 113702. DOI: 10.1088/1674-1056/25/11/113702

Fast thermometry for trapped atoms using recoil-induced resonance

Zhao Yan-Ting (赵延霆), Su Dian-Qiang (苏殿强), Ji Zhong-Hua (姬中华), Zhang Hong-Shan (张洪山), Xiao Lian-Tuan (肖连团), Jia Suo-Tang (贾锁堂)
Chin. Phys. B, 2015, 24 (**9**): 093701. DOI: 10.1088/1674-1056/24/9/093701

Conditions for formation and trapping of the two-ion Coulomb cluster in the dissipative optical superlattice

I. V. Krasnov
Chin. Phys. B, 2015, 24 (**6**): 063701. DOI: 10.1088/1674-1056/24/6/063701

SPECIAL TOPIC — Advances in thorium nuclear optical clocks

Prediction of $I_g, 6d_{3/2} \rightarrow I_g, 7p_{1/2}$, $I_g, 7s_{1/2} \rightarrow I_g, 7p_{1/2}$ and $I_g, 7p_{1/2} \rightarrow I_m, 7s_{1/2}$ transition frequencies in $^{229}Th^{3+}$ ion

Shi-Cheng Yu(余师成)[1,2], Cheng-Bin Li(李承斌)[1,†], and Lei She(佘磊)[1,3,‡]

[1] *Key Laboratory of Atomic Frequency Standards, Innovation Academy for Precision Measurement Science and Technology, Chinese Academy of Sciences, Wuhan* 430071, *China*

[2] *University of Chinese Academy of Sciences, Beijing* 100049, *China*

[3] *Wuhan Institute of Quantum Technology, Wuhan* 430206, *China*

(Received 26 May 2025; revised manuscript received 14 August 2025; accepted manuscript online 28 August 2025)

The ^{229}Th nucleus has attracted considerable attention due to the existence of its low-energy isomeric state; however, direct laser excitation in ionic systems poses significant challenges for current laser technologies. In the $^{229}Th^{3+}$ ion, the electronic bridge (EB) process enables the conversion of direct laser excitation into an effective two-photon process ($I_g, 6d_{3/2} \rightarrow I_g, 7p_{1/2} \rightarrow I_m, 7s_{1/2}$), thereby circumventing the requirement for laser radiation at 148 nm. In this work, we employ many-body perturbation theory (MBPT) to calculate the hyperfine structure constants and field shift factors for several low-lying excited states of the $^{229}Th^{3+}$ ion. By combining these theoretical results with previously reported experimental data, we predict three transition frequencies associated with the EB process in the $^{229}Th^{3+}$ ion and identify the most suitable transition pathway for EB-assisted nuclear excitation.

Keywords: thorium nuclear clock, electronic bridge process, nuclear hyperfine mixing

PACS: 37.10.Vz, 31.15.–p, 31.15.am, 31.30.Gs

DOI: 10.1088/1674-1056/ae0016 **CSTR:** 32038.14.CPB.ae0016

1. Introduction

As precision measurement tools, optical clocks fulfill critical roles spanning from global positioning systems to fundamental physics research.[1] The ^{229}Th nucleus has emerged as a leading candidate for next-generation nuclear optical clocks, featuring a low-energy ($\approx$ 8.3 eV) nuclear transition, a sub-mHz natural linewidth, intrinsic immunity to external perturbations, and heightened sensitivity to temporal variations of the fine-structure constant.[2–5]

Direct laser excitation of the ^{229}Th nucleus presents formidable challenges for current deep ultraviolet (XUV) laser technologies. Breakthroughs in solid-state approaches have demonstrated nuclear excitation in Th-doped crystals and thin films,[6–10] where the host material confines nuclei in motional ground states without requiring cooling lasers. This confinement mechanism, combined with the high nuclear density ($\sim 10^{18}$ cm^{-3}) in crystalline matrices, greatly enhances the signal-to-noise ratio compared to ion trap systems.[11,12] The success of these solid-state platforms establishes a viable pathway toward compact nuclear optical clocks, significantly simplifying the laser architecture by eliminating auxiliary cooling and other lasers.[13]

Ionic nuclear clocks offer unprecedented precision potential, with theoretical predictions achieving 10^{-19} level accuracy through relativistic atomic structure calculations and well-defined nuclear–electronic coupling models.[14,15] High-precision spectra of several Th ions, capable of resolving ultrafine states, serve as probes for extracting nuclear structure information. The combination of high-precision relativistic theoretical calculations and spectroscopic measurements has enabled the extraction of several nuclear structural parameters, including the α-sensitivity,[16] nuclear charge radius,[17–19] electric quadrupole moment, and magnetic dipole moment.[20]

Additionally, nuclear hyperfine mixing (NHM) enables two-photon excitation through electronic bridge (EB) processes, bypassing the 148 nm laser requirement.[21,22] The $^{229}Th^{3+}$ ion provides an ideal platform for nuclear excitation via EB processes: (i) its simplified electronic configuration minimizes competing relaxation channels; (ii) its moderate ionization potential ensures that $^{229}Th^{3+}$ ions can be directly produced by laser sputtering; (iii) the required transition wavelengths fall within commercially available laser ranges.

Figure 1 schematically illustrates key transitions in the EB process of $^{229}Th^{3+}$. Transition wavelengths are derived from experimental measurements of $^{232}Th^{3+}$ ions,[23] natural linewidths are calculated using relativistic coupled-cluster methods,[24] and EB transition linewidths incorporate both the ^{229}Th nuclear isomer lifetime[25] and EB enhancement fac-

†Corresponding author. E-mail: cbli@apm.ac.cn

‡Corresponding author. E-mail: shelei@apm.ac.cn

© 2026 Chinese Physical Society and IOP Publishing Ltd. All rights, including for text and data mining, AI training, and similar technologies, are reserved.

tor calculations.[21] The $^{229}Th^{3+}$ ion has a $5f_{5/2}$ ground state, which is excited to the $6d_{3/2}$ state via 1088 nm laser pumping, followed by 196 nm laser preparation into the metastable $7s_{1/2}$ state. The 0.6 s lifetime of this metastable state enables two-photon EB excitation (269 nm plus 330 nm). In this work, we predict three transition frequencies in Fig. 1 by combining many-body perturbation theory (MBPT)-calculated hyperfine structure constants and field shift factors with existing experimental values. We also identify the most suitable transition pathway to reduce laser power requirements and laser-induced ion heating. These results provide critical guidance for realizing EB-mediated nuclear excitation in $^{229}Th^{3+}$.

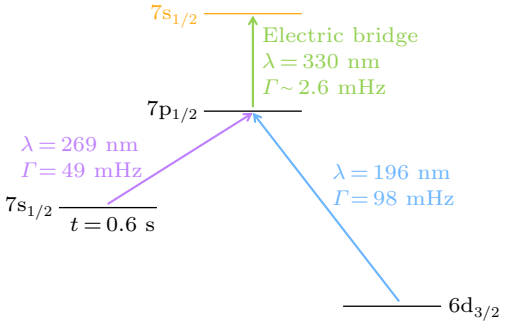


Fig. 1. Schematic energy level diagram of $^{229}Th^{3+}$ ions. Orange-colored levels represent the nuclear isomer state (I_m), while black-filled levels correspond to the nuclear ground state (I_g). Transitions are labeled with the corresponding wavelengths λ and natural linewidths Γ. References for these transition properties are provided in the main text.

2. Method

The relativistic many-body perturbation theory implementation in this work utilizes the AMBiT package. Our treatment of core–valence electron correlations employs the second-order self-energy approximation $\Sigma^{(2)}(E)$ within the Brillouin–Wigner formalism. The governing equation for the valence-electron eigenvalue problem is expressed as

$$\left[\hat{H}+\Sigma^{(2)}(E)\right]|\psi\rangle = E|\psi\rangle, \tag{1}$$

with the Dirac–Fock Hamiltonian defined by

$$\hat{H} = c\boldsymbol{\alpha}\cdot\boldsymbol{p}+(\beta-1)mc^2+V_{\rm nuc}(r)+V^{N-1}. \tag{2}$$

Here $V_{\rm nuc}(r)$ represents the finite-nucleus potential (Fermi distribution model), while V^{N-1} characterizes the direct and exchange interaction between core electrons and the valence electron. Single-particle orbitals are generated through the Dirac–Fock procedure in the V^{N-1} potential.

The model space P comprises Slater determinants $|I\rangle$ with fixed core configurations. The eigenstate expansion takes the form

$$|\psi\rangle = \sum_{I\in P} C_I|I\rangle. \tag{3}$$

The energy-dependent self-energy operator $\Sigma^{(2)}(E)$ in matrix representation becomes

$$\Sigma^{(2)}_{IJ}(E) = \sum_{M\in Q}\frac{\langle I|H|M\rangle\langle M|H|J\rangle}{E-E_M}, \tag{4}$$

where $|M\rangle$ denotes intermediate states in the complementary space Q containing core-excited configurations. The complete Hilbert space $\mathcal{H}$ satisfies the decomposition $P\oplus Q=\mathcal{H}$. Diagrammatic analysis confirms that single-valence excitations exclusively contribute to $\Sigma^{(2)}(E)$ in monovalent systems.

The resulting nonlinear eigenvalue problem is formulated as

$$\sum_{J\in P}\left[H_{IJ}+\sum_{M\in Q}\frac{H_{IM}H_{MJ}}{E-E_M}\right]C_J = EC_I. \tag{5}$$

For the $^{229}Th^{3+}$ ion system, significant higher-order correlation effects necessitate scaling adjustments to the second-order correlation operator. We introduce a κ-dependent scaling factor λ_κ to modify the operator matrix elements, enabling improved agreement between calculated energy levels and experimental spectroscopic data

$$\hat{H}+\Sigma^{(2)}(E)\to\hat{H}+\lambda_\kappa\Sigma^{(2)}(E). \tag{6}$$

The scaling factor can be calculated as

$$\lambda \approx \frac{E_{\rm expt}-E_{\rm DF}}{E_{\rm MBPT}-E_{\rm DF}}. \tag{7}$$

The random-phase approximation (RPA) is also taken into account in the calculation of matrix elements[26]

$$(\hat{H}-E_c)|\delta c\rangle = -(\hat{O}+\delta V_{\rm core})|c\rangle, \tag{8}$$

where $\hat{O}$ is the operator corresponding to the physical quantities of interest, and $|c\rangle$ and $|\delta c\rangle$ represent the core-electron states and their corrections induced by the operator $\hat{O}$, respectively. The term $\delta V_{\rm core}$ denotes the change in V^{N-1} arising from the variation of the core-electron states and is included in the calculation of matrix elements

$$\langle i|\hat{O}|j\rangle\to\langle i|\hat{O}+\delta V_{\rm core}|j\rangle. \tag{9}$$

In our calculation, we use 50 B-splines of order $k=11$ and set $R_{\rm max}=50a_0$, which is sufficient to describe the behavior of wavefunctions of the low-lying excited states, as shown in Fig. 2. We expand the true eigenstate using 20spdf orbitals, and 30spdfghi orbitals are employed for the calculation of the self-energy operator $\Sigma^{(2)}(E)$. The Breit interaction is taken into account.

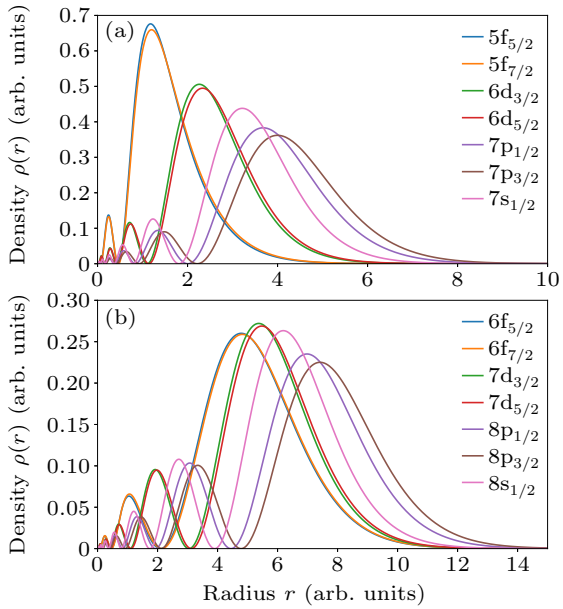


Fig. 2. Radial density distributions of the valence electron in low-lying states.

3. Results

3.1. Atomic structure

Firstly, we demonstrate the reliability of our calculations. Table 1 presents our calculated energies obtained from three different computational models: Dirac–Fock, MBPT, and MBPT with scaling. The Dirac–Fock model fails to reproduce the correct ordering of energy levels, whereas the MBPT model captures electron-correlation effects more accurately and therefore yields the correct sequence of energy levels. For the lowest state of each angular momentum J, the deviation amounts to several thousand wavenumbers, while for the second state of each angular momentum J, the deviation is reduced to several hundred wavenumbers.

Table 1. Energies of low-lying states in the $^{229}Th^{3+}$ ion (in units of cm^{-1}). The subscripts "DF", "MBPT", "sc", and "expt" correspond to energies calculated using the Dirac–Fock method, MBPT, MBPT with scaling, and experimental values[23], respectively. $\delta E = E - E_{expt}$.

Config.	E_{DF}	E_{MBPT}	E_{sc}	E_{expt}	δE_{MBPT}	δE_{sc}
$5f_{5/2}$	−207309	−238617	−230976	−231065	−7552	89
$5f_{7/2}$	−203993	−233823	−226648	−226740	−7083	92
$6d_{3/2}$	−211842	−224858	−221838	−221872	−2986	34
$6d_{5/2}$	−207686	−219070	−216550	−216579	−2491	29
$7s_{1/2}$	−200183	−211706	−207837	−207934	−3771	97
$7p_{1/2}$	−164931	−173239	−170739	−170826	−2413	87
$7p_{3/2}$	−153506	−159959	−157942	−158009	−1950	67
$8s_{1/2}$	−109163	−112377	−111325	−111443	−934	118
$7d_{3/2}$	−108633	−111560	−110877	−111380	−179	504
$7d_{5/2}$	−107048	−109813	−109196	−109638	−175	442
$6f_{5/2}$	−99982	−104139	−103099	−103796	−343	696
$6f_{7/2}$	−99561	−103670	−102661	−103250	−421	589
$8p_{1/2}$	−94525	−97225	−96434	−96549	−677	114
$8p_{3/2}$	−89565	−91820	−91131	−91194	−626	63

To reduce the error in the energy-level calculations, as discussed in Section 2, we introduce a scaling factor to match the energies of the first state under each angular momentum to the experimental results. After introducing the scaling factor, the error in the energy of the first state under each angular momentum is reduced to a few dozen wavenumbers. The error in the energy of the second state under each angular momentum is increased, but it remains at the level of several hundred wavenumbers. The values of the scaling factors are as follows:

$$\lambda_{s_{1/2}} = 0.673,\ \lambda_{p_{1/2}} = 0.710,\ \lambda_{p_{3/2}} = 0.698,$$
$$\lambda_{d_{3/2}} = 0.771,\ \lambda_{d_{5/2}} = 0.781,\ \lambda_{f_{5/2}} = 0.759,$$
$$\lambda_{f_{7/2}} = 0.763.$$

Although the scaling factor has a significant influence on the energy levels, its introduction leads to only a few-percent change in the calculated matrix elements of other operators, which is much smaller than the correction introduced by the RPA. In the subsequent results, we include the RPA correction throughout.

Table 2. Hyperfine structure constants A in units of MHz for low-lying states of the nuclear ground state ($I_g = 5/2$ and $\mu_g = 0.366(6)\ \mu_N$[20]). The subscripts "sc" and "expt" correspond to results obtained using MBPT with scaling and experimental measurements,[27] respectively. The uncertainties are given in parentheses.

Config.	A_{sc}	A_{expt}	Diff. (%)
$5f_{5/2}$	72.46	82.2(6)	13.4%
$5f_{7/2}$	27.53	31.4(7)	14.1%
$6d_{3/2}$	135.78	155.3(1.2)	14.4%
$6d_{5/2}$	−43.83	−12.6(7)	71.3%
$7s_{1/2}$	6111(878)		
$7p_{1/2}$	1436(206)		

We present the calculated hyperfine structure constants A in Table 2 and compare them with experimental measurements. Our results show deviations of approximately 14% from the experimental values. However, for the $6d_{5/2}$ state, the deviation reaches 71%. We note that this behavior is not unique to our calculations. In relativistic coupled-cluster (RCC) calculations,[28] the deviation of the hyperfine structure constant for this state is significantly larger than that for other states. The substantial discrepancy in the hyperfine structure constant for this state obtained using two distinct RCC methods suggests a high sensitivity to higher-order correlation effects.[29]

Therefore, the deviation of the $6d_{5/2}$ state from the experimental values is not adopted. Instead, we select the maximum deviation of 14.4% as the uncertainty of the hyperfine structure constants A for the $7s_{1/2}$ and $7p_{1/2}$ states. As a further verification of the calculation accuracy, the calculated hyperfine structure constants B for the $5f_{5/2,7/2}$ and $6d_{3/2,5/2}$ states show deviations from the experimental values at the 3% level.

The calculated field shift factors are listed in Table 3 and compared with results obtained from relativistic coupled-

cluster (RCC) calculations.[26] Our results show good agreement with those from RCC, demonstrating that MBPT can accurately capture the essential features of electron-correlation corrections. In the subsequent calculations, we adopt the RCC results. The uncertainties are estimated as the differences between the RCC results and our MBPT values.

Table 3. Field shift factors FS in units of GHz/fm^2 for low-lying states in the ^{229}Th^{3+} ion. The subscripts "DF" and "sc" correspond to results obtained using the Dirac–Fock method and MBPT with scaling, respectively.

Config.	$FS_{\rm DF}$	$FS_{\rm sc}$	Ref. [26]
$5f_{5/2}$	−51.0	−53.6	−55.0
$5f_{7/2}$	−48.9	−51.6	−53.0
$6d_{3/2}$	−21.8	−22.9	−23.3
$6d_{5/2}$	−19.0	−19.9	−20.5
$7s_{1/2}$	83.7	91.5	92.1
$7p_{1/2}$	2.2	2.5	2.7

3.2. Frequency prediction

Transition frequencies in ^{229}Th^{3+} are predicted via isotope shifts relative to ^{232}Th^{3+} spectroscopic data, incorporating hyperfine-structure corrections

$$\nu^{229}_{i\to j} = \nu^{232}_{i\to j} + \Delta\nu_{\rm IS} + \Delta W, \tag{10}$$

where i and j denote the initial and final states of the transition, $\Delta\nu_{\rm IS}$ represents the isotope shift, and ΔW arises from hyperfine structure.

The isotope shifts are calculated as

$$\Delta\nu_{\rm IS} \approx (FS_j - FS_i)(\langle r^2_{229g}\rangle - \langle r^2_{232}\rangle), \tag{11}$$

where FS denotes the field shift factor and $\langle r^2\rangle$ is the nuclear mean-square charge radius. Here, we neglect the isotope shift arising from changes in nuclear mass. For heavy elements, the contribution of this term is much smaller than that of the dominant field shift. In Table 4, we present the calculated isotope shifts and compare them with experimental values. The maximum deviation is found to be 4%, which lies within the estimated uncertainty of the calculation.

Table 4. Isotope shifts $\Delta\nu_{\rm IS}$ in units of MHz between low-lying states from ^{232}Th to ^{229g}Th ($\langle r^2_{229g}\rangle - \langle r^2_{232}\rangle = -0.299(15)$ fm^2[17]). The subscripts "sc" and "expt" correspond to results obtained using MBPT with scaling and experimental measurements,[27] respectively. The uncertainties are given in parentheses.

Transi.	$\Delta\nu_{\rm sc}$	$\Delta\nu_{\rm expt}$	Diff. (%)
$5f_{5/2}\to 6d_{3/2}$	−9748(651)	−9856(10)	4.0%
$5f_{5/2}\to 6d_{5/2}$	−10386(619)	−10509(7)	1.9%
$5f_{7/2}\to 6d_{5/2}$	−9718(664)	−9890(9)	1.8%
$6d_{3/2}\to 7p_{1/2}$	−7774(416)		
$7s_{1/2}\to 7p_{1/2}$	26731(1356)		

The transition frequencies of $6d_{3/2}\to 7p_{1/2}$ and $7s_{1/2}\to 7p_{1/2}$ in ^{232}Th^{3+} are measured as 195.903 nm and 269.481 nm, respectively,[23] corresponding to the following frequencies:

$$\nu^{232}_{6d_{3/2}\to 7p_{1/2}} = 1530309\ \text{GHz}, \tag{12}$$

$$\nu^{232}_{7s_{1/2}\to 7p_{1/2}} = 1112475\ \text{GHz}. \tag{13}$$

In Ref. [23], a general uncertainty of 0.0005 nm was assigned to both transition frequencies without detailed analysis. Another Ref. [30] reported a high-precision measurement of the $6d_{3/2}\to 7s_{1/2}$ transition frequency, with an uncertainty of 30 MHz. This transition frequency can be derived by taking the difference between the two transition frequencies in Eq. (12), which reveals a discrepancy of 12 GHz. This deviation significantly exceeds the uncertainty reported in Ref. [23]. In the present work, we re-estimate the uncertainties of these two transitions as 12 GHz, based on the comparison between the two references.

Adding the isotope shifts shown in Table 4

$$\nu^{229,c}_{6d_{3/2}\to 7p_{1/2}} = 1530301(12)\ \text{GHz}, \tag{14}$$

$$\nu^{229,c}_{7s_{1/2}\to 7p_{1/2}} = 1112502(12)\ \text{GHz}, \tag{15}$$

where the superscript c represents the central frequency without hyperfine splitting.

The hyperfine shift ΔW can be calculated as

$$\Delta W = W_{j,F_j} - W_{i,F_i}, \tag{16}$$

where W_{i,F_i} represents the hyperfine splitting of state i with total angular momentum quantum number F_i

$$W_{i,F_i} = \frac{1}{2}K_iA_i + \frac{1}{2}\frac{3K_i(K_i+1) - 4J_i(J_i+1)I_i(I_i+1)}{2I_i(2I_i-1)2J_i(2J_i-1)}B_i, \tag{17}$$

where $K_i = F_i(F_i+1) - I_i(I_i+1) - J_i(J_i+1)$. The meaning of W_{j,F_j} is analogous to W_{i,F_i}.

Table 5. Predicted hyperfine splitting shifts ΔW and transition frequencies for the $I_g, 6d_{3/2}\to I_g, 7p_{1/2}$ transition. $F_{\rm l}$ and $F_{\rm h}$ denote the quantum numbers F for the $6d_{3/2}$ and $7p_{1/2}$ states, respectively. Uncertainties are given in parentheses.

$F_{\rm l}$	$F_{\rm h}$	ΔW (MHz)	Freq. (GHz)
1	2	−3283(316)	1530298(12)
2	2	−1781(316)	1530299(12)
2	3	2526(226)	1530304(12)
3	2	−1228(316)	1530300(12)
3	3	3079(226)	1530304(12)
4	3	646(226)	1530302(12)

Table 6. Predicted hyperfine splitting shifts ΔW and total transition frequencies for the $I_g, 7s_{1/2}\to I_g, 7p_{1/2}$ transition. $F_{\rm l}$ and $F_{\rm h}$ denote the quantum numbers F for the $7s_{1/2}$ and $7p_{1/2}$ states, respectively. Uncertainties are given in parentheses.

$F_{\rm l}$	$F_{\rm h}$	ΔW (MHz)	Freq. (GHz)
2	2	8182(1380)	1112510(12)
2	3	12488(1363)	1112514(12)
3	2	−10151(1010)	1112492(12)
3	3	−5844(986)	1112496(12)

Based on the experimental measurements for hyperfine structure constants of the $I_g, 6d_{3/2}$ state and the calculated hyperfine structure constants of the $I_g, 7s_{1/2}$ and $I_g, 7p_{1/2}$ states, the total transition frequencies of $I_g, 6d_{3/2} \to I_g, 7p_{1/2}$ and $I_g, 7s_{1/2} \to I_g, 7p_{1/2}$ can be calculated. The results are shown in Tables 5 and 6, and the uncertainties are dominated by the spectroscopic measurements of $^{232}Th^{3+}$.

Next, we predict the frequency of the EB transition. The nuclear transition frequencies have been measured with kHz-level accuracy in Th-doped solids.[9] Since in Th-doped solids, the four electrons of neutral Th atoms are compensated by the surrounding F atoms, the nuclear transition frequency in the Th-doped solid can be regarded as that of the $^{229}Th^{4+}$ ion

$$\nu_N(\mathrm{Th}_g^{4+}) = 2020407384.335(2)\ \mathrm{MHz}, \tag{18}$$

where g represents the $^{229}Th^{4+}$ ion in the ground state.

Since nuclear transitions change the nuclear charge radius, the field shift that depends on the electronic structure will cause a difference $\Delta\nu_N$ in the nuclear transition frequencies under different electronic configurations

$$\nu_N^c(\mathrm{Th}_{7s_{1/2}}^{3+}) = \nu_N(\mathrm{Th}_g^{4+}) + \Delta\nu_N, \tag{19}$$

where

$$\Delta\nu_N = \left[FS(\mathrm{Th}_{7s_{1/2}}^{3+}) - FS(\mathrm{Th}_g^{4+})\right] \times \delta\langle r^2\rangle^{229m,229}. \tag{20}$$

In MBPT calculations of field shift factors, contributions from core electrons are not included; hence we can directly use the values in Table 3 to approximate $FS(\mathrm{Th}_{7s_{1/2}}^{3+}) - FS(\mathrm{Th}_g^{4+})$. The RPA correction validates this approximation. For example, multiconfiguration Dirac–Hartree–Fock calculations show $FS(\mathrm{Th}_{5f_{5/2}}^{3+}) - FS(\mathrm{Th}_g^{4+}) = -57.1$ GHz/fm^2,[31] which is close to our result -53.6 GHz/fm^2 and the RCC result -55.0 GHz/fm^2.[26] As a result, combining $\delta\langle r^2\rangle^{229m,229} = 0.0105(13)$ fm^2,[17] the central frequency of the nuclear transition in $^{229}Th^{3+}(7s_{1/2})$ is

$$\nu_N^c(\mathrm{Th}_{7s_{1/2}}^{3+}) = 2020408351(120)\ \mathrm{MHz}. \tag{21}$$

The central frequency of the EB transition can also be obtained, with the uncertainty still dominated by the spectroscopic measurements of $^{232}Th^{3+}$

$$\nu_{EB}^c = \nu_N^c(\mathrm{Th}_{7s_{1/2}}^{3+}) - \nu_{7s_{1/2}\to 7p_{1/2}}^{229,c} = 907907(12)\ \mathrm{GHz}. \tag{22}$$

By determining the hyperfine structure constant A of the $^{229m}Th^{3+}(7s_{1/2})$ state, the hyperfine splitting shift ΔW of the EB transition frequency can be calculated. Combining the measurements for the hyperfine structure constant A of $^{229m}Th^{3+}(6d_{3/2})$[25] and $^{229}Th^{3+}(6d_{3/2})$,[27] an improved ratio of nuclear magnetic moments is obtained

$$\mu_m/\mu_g = -1.016(14), \tag{23}$$

which increases the precision tenfold compared to the previous result $\mu_m/\mu_g = -1.04(15)$.[18] Based on this new ratio, we predict that the hyperfine structure constant A of the $^{229m}Th^{3+}(7s_{1/2})$ state is $-10349(1308)$ MHz. The total frequencies of the EB transition are shown in Table 7.

Table 7. Predicted hyperfine splitting shifts ΔW and total transition frequencies for the $I_g, 7p_{1/2} \to I_m, 7s_{1/2}$ EB transition. F_l and F_h denote the quantum numbers F for the $7p_{1/2}$ and $7s_{1/2}$ states, respectively. Uncertainties are given in parentheses.

F_l	F_h	ΔW (MHz)	Freq. (GHz)
2	1	15448(1666)	907922(12)
2	2	−5249(1031)	90701(12)
3	2	−9556(1007)	907897(12)

3.3. EB transition

The NHM effect arises from the electromagnetic interaction between the nucleus and bound electrons, which can be described by the total Hamiltonian[32,33]

$$H = H_e + H_n + H_{en}, \tag{24}$$

$$H_{en} = \sum_{\tau=E,M}\sum_{Lm}(-1)^m M_{L,-m}^{\tau} T_{Lm}^{\tau}, \tag{25}$$

where H_e and H_n are the Hamiltonians of the electrons and the nucleus, respectively, and M_{Lm}^{τ} (T_{Lm}^{τ}) are the nuclear (electronic) multipole operators of rank L.

In the coupled basis $|FM_F(I\gamma J)\rangle$, NHM can be treated perturbatively as

$$\underline{|F_\mu M_{F_\mu}\rangle} = |F_\mu M_{F_\mu}\rangle + \sum_{\mu'\varepsilon'} b_{\mu\varepsilon;\mu'\varepsilon'} \left|FM_F(I_{\mu'}\gamma_{\varepsilon'}J_{\varepsilon'})\right\rangle, \tag{26}$$

$$b_{\mu\varepsilon;\mu'\varepsilon'} = \frac{(-1)^{I_\mu+J_{\varepsilon'}+F}}{E_{\mu\varepsilon}-E_{\mu'\varepsilon'}} \sum_{L\tau} \begin{Bmatrix} I_{\mu'} & J_{\varepsilon'} & F \\ J_\varepsilon & I_\mu & L \end{Bmatrix} \times \langle I_{\mu'}\|M_L^{\tau}\|I_\mu\rangle\langle\gamma_{\varepsilon'}J_{\varepsilon'}\|T_L^{\tau}\|\gamma_\varepsilon J_\varepsilon\rangle. \tag{27}$$

Here, the underline denotes states corrected by hyperfine interactions, $b_{\mu\varepsilon;\mu'\varepsilon'}$ quantifies the mixing between different nuclear and electronic states (enabling otherwise forbidden nuclear transition channels), and γ represents other quantum numbers.

In the $^{229}Th^{3+}$ ion, there exists an electronic transition $7s_{1/2} \to 8s_{1/2}$ whose frequency is close to that of the nuclear transition. In the NHM calculation for the state $|I_m, 7s_{1/2}\rangle$, contributions from other states are negligible compared to the state $|I_g, 8s_{1/2}\rangle$. Moreover, the ^{229}Th nuclear transition is dominated by the $M1$ channel. Therefore, the summation in the general NHM expression can be simplified as

$$\underline{|7s_{1/2}, I_m, F, M_F\rangle} = |7s_{1/2}, I_m, F, M_F\rangle + b(F)|8s_{1/2}, I_g, F, M_F\rangle, \tag{28}$$

$$b(F) = (-1)^{I_m+1/2+F}\langle I_g\|M1\|I_m\rangle \times \begin{Bmatrix} I_g & 1/2 & F \\ 1/2 & I_m & 1 \end{Bmatrix} \frac{\langle 8s_{1/2}\|T_1\|7s_{1/2}\rangle}{\omega_N - \omega_{8s_{1/2},7s_{1/2}}}, \tag{29}$$

where $M1$ is the magnetic dipole transition operator, T_1 is the magnetic dipole hyperfine interaction operator, $\omega_{\rm N}$ is the nuclear transition energy, and $\omega_{i,j} = \varepsilon_i - \varepsilon_j$.

The nuclear matrix element $\langle I_{\rm g}||M_1||I_{\rm m}\rangle$ is related to the lifetime of the nuclear isomer state ($\tau = 641$ s in crystal, refractive index $n \approx 1.586$),[7,9] corresponding to $\langle I_{\rm g}||M_1||I_{\rm m}\rangle = 1.59 \times 10^{-6}$ a.u. The matrix element $\langle 8{\rm s}_{1/2}||T_1||7{\rm s}_{1/2}\rangle = -0.9391$ is calculated using MBPT with scaling plus RPA. Based on our previous uncertainty analysis of the hyperfine constant A, we estimate the uncertainty of this value to be 14.4%. As a result, the absolute value of the mixing coefficient is

$$|b(2)| = 2.91(42) \times 10^{-6}. \tag{30}$$

Due to angular momentum coupling, the NHM effect exists only for $F = 2$.

Hence, the matrix element of the EB transition can be expressed as

$$\begin{aligned}&\langle 7{\rm p}_{1/2}, I_{\rm g}, F, M_1|E1|\underline{7{\rm s}_{1/2}, I_{\rm m}, 2, M_2}\rangle \\ &= b(2)\langle 7{\rm p}_{1/2}, I_{\rm g}, F, M_1|E1|8{\rm s}_{1/2}, I_{\rm g}, 2, M_2\rangle,\end{aligned} \tag{31}$$

where $E1$ is the electric dipole transition operator.

We calculate the EB matrix element by combining the reduced matrix elements in F-space with the Wigner–Eckart theorem

$$\begin{aligned}|\langle FM_F|E1|F'M_F'\rangle| = &\left|\begin{pmatrix} F & 1 & F' \\ -M_F & q & M_F' \end{pmatrix}\sqrt{(2F+1)(2F'+1)}\right. \\ &\left.\times \begin{Bmatrix} F & 1 & F' \\ J' & I_{\rm g} & J \end{Bmatrix}\langle J||E1||J'\rangle\right|.\end{aligned} \tag{32}$$

The reduced matrix element $\langle 7{\rm p}_{1/2}||E1||8{\rm s}_{1/2}\rangle = 1.5610$ a.u., calculated by the RCC method,[24] yielding the maximum EB matrix element

$$|\langle 7{\rm p}_{1/2}, I_{\rm g}, 3, \pm 3|E1|\underline{7{\rm s}_{1/2}, I_{\rm m}, 2, \pm 2}\rangle| = 2.39(34) \times 10^{-6}\ \text{a.u.} \tag{33}$$

Table 8. Laser intensity ratios for different hyperfine states of $I_{\rm g}, 7{\rm s}_{1/2}$. Here, I_{330} denotes the laser intensity for the EB transition, and I_{269} denotes the laser intensity for the $I_{\rm g}, 7{\rm s}_{1/2} \to I_{\rm g}, 7{\rm p}_{1/2}$ transition. The reduced matrix element $\langle 7{\rm s}_{1/2}||E1||7{\rm p}_{1/2}\rangle = 2.4375$ a.u., calculated using the RCC method.[24]

F	M_F	Ratio I_{330}/I_{269}
2	± 2	$2.88(83) \times 10^{11}$
3	± 3	$1.73(50) \times 10^{11}$
3	± 2	$5.76(166) \times 10^{10}$

Reference literature indicates that, for efficient EB nuclear excitation, the Rabi frequencies of the $I_{\rm g}, 7{\rm s}_{1/2} \to I_{\rm g}, 7{\rm p}_{1/2}$ transition (269 nm) and EB transition (330 nm) should be equal to achieve the maximum excitation efficiency of 27.9%.[32] Since the Rabi frequency $\Omega \propto \sqrt{I_\ell} D$ for a Gaussian beam (I_ℓ is the laser intensity and D is the transition matrix element),[34] the ratio of the two laser intensities should be inversely proportional to the square of the ratio of the transition matrix elements. These ratios are presented in Table 8.

In the experiment, the strongest EB transition and the weakest $I_{\rm g}, 7{\rm s}_{1/2} \to I_{\rm g}, 7{\rm p}_{1/2}$ transition should be selected as much as possible to reduce the requirement for laser power and the heating of ions by the laser. Therefore, we recommend using the following transition path to achieve EB nuclear excitation:

$$\begin{aligned}&|I_{\rm g}, 7{\rm s}_{1/2}, F = 3, M_F = \pm 2\rangle \\ \to\ &|I_{\rm g}, 7{\rm p}_{1/2}, F = 3, M_F = \pm 3\rangle \\ \to\ &|I_{\rm m}, 7{\rm s}_{1/2}, F = 2, M_F = \pm 2\rangle.\end{aligned} \tag{34}$$

4. Conclusion

In conclusion, we employed the MBPT + RPA method to calculate the hyperfine structure constants and field shift factors of low-lying excited states of Th^{3+}, providing a detailed uncertainty analysis. We also predicted the laser frequency ranges required to achieve EB nuclear excitation. Additionally, we calculated the matrix elements of the EB transition including hyperfine coupling and recommended a suitable transition path for achieving EB nuclear excitation.

Acknowledgments

This work was supported by the Strategic Priority Research Program of the Chinese Academy of Sciences (Grant No. XDB0920403) and the National Key Research and Development Program of China (Grant No. 2022YFB3904002).

References

[1] Ludlow A D, Boyd M M, Ye J, Peik E and Schmidt P 2015 *Rev. Mod. Phys.* **87** 637
[2] Tkalya E, Varlamov V, Lomonosov V and Nikulin S 1996 *Phys. Scr.* **53** 296
[3] Peik E and Tamm C 2003 *Europhys. Lett.* **61** 181
[4] Thirolf P G, Kraemer S, Moritz D and Scharl K 2024 *Eur. Phys. J. Spec. Top.* **233** 1113
[5] Tong X, Hua L, Hua X and Liu X 2025 *Natl. Sci. Rev.* nwaf083
[6] Nickerson B S, Pimon M, Bilous P V, Gugler J, Beeks K, Sikorsky T, Mohn P, Schumm T and Pálffy A 2020 *Phys. Rev. Lett.* **125** 032501
[7] Tiedau J, Okhapkin M, Zhang K, Thielking J, Zitzer G, Peik E, Schaden F, Pronebner T, Morawetz I, De Col L T, Schneider F, Leitner A, Pressler M, Kazakov G, Beeks K, Sikorsky T and Schumm T 2024 *Phys. Rev. Lett.* **132** 182501
[8] Elwell R, Schneider C, Jeet J, Terhune J, Morgan H, Alexandrova A, Tran Tan H, Derevianko A and Hudson E R 2024 *Phys. Rev. Lett.* **133** 013201
[9] Zhang C, Ooi T, Higgins J S, Doyle J F, *et al*. 2024 *Nature* **633** 63
[10] Zhang C, von der Wense L, Doyle J F, *et al*. 2024 *Nature* **636** 603
[11] Jackson R A, Amaral J B, Valerio M E G, DeMille D P and Hudson E R 2009 *J. Phys. Condens. Matt.* **21** 325403
[12] Dessovic P, Mohn P, Jackson R A, Winkler G, Schreitl M, Kazakov G and Schumm T 2014 *J. Phys. Condens. Matt.* **26** 105402

[13] Kazakov G A, Litvinov A N, Romanenko V I, Yatsenko L P, Romanenko A V, Schreitl M, Winkler G and Schumm T 2012 *New J. Phys.* **14** 083019

[14] Campbell C J, Radnaev A G, Kuzmich A, Dzuba V A, Flambaum V V and Derevianko A 2012 *Phys. Rev. Lett.* **108** 120802

[15] Beloy K 2023 *Phys. Rev. Lett.* **130** 103201

[16] Beeks K, Kazakov G A, Schaden F, *et al.* 2025 *Nat. Commun.* **16** 9147

[17] Safronova M, Porsev S, Kozlov M, Thielking J, Okhapkin M, Głowacki P, Meier D and Peik E 2018 *Phys. Rev. Lett.* **121** 213001

[18] Thielking J, Okhapkin M V, Głowacki P, Meier D M, Von Der Wense L, Seiferle B, Düllmann C E, Thirolf P G and Peik E 2018 *Nature* **556** 321

[19] Kälber W, Rink J, Bekk K, Faubel W, Göring S, Meisel G, Rebel H and Thompson R C 1989 *Z. Phys. A* **334** 103

[20] Porsev S, Safronova M and Kozlov M 2021 *Phys. Rev. Lett.* **127** 253001

[21] Porsev S G and Flambaum V V 2010 *Phys. Rev. A* **81** 032504

[22] Li L, Li Z, Wang C, Gan W T, Hua X and Tong X 2023 *Nucl. Sci. Technol.* **34** 24

[23] Klinkenberg P F A 1988 *Physica B+C* **151** 552

[24] Li F C, Qiao H X, Tang Y B and Shi T Y 2022 *J. Quant. Spectrosc. Radiat. Transfer* **288** 108241

[25] Yamaguchi A, Shigekawa Y, Haba H, Kikunaga H, Shirasaki K, Wada M and Katori H 2024 *Nature* **629** 62

[26] Dzuba V and Flambaum V 2023 *Phys. Rev. Lett.* **131** 263002

[27] Campbell C J, Radnaev A G and Kuzmich A 2011 *Phys. Rev. Lett.* **106** 223001

[28] Safronova M S, Safronova U I, Radnaev A G, Campbell C J and Kuzmich A 2013 *Phys. Rev. A* **88** 060501

[29] Li F C, Qiao H X, Tang Y B and Shi T Y 2021 *Phys. Rev. A* **104** 062808

[30] Radnaev A G, Campbell C J and Kuzmich A 2012 *Phys. Rev. A* **86** 060501

[31] Si R, Shi C, Xue N, Kong X, Chen C, Tu B and Ma Y G 2025 *Sci. China Phys. Mech. Astron.* **68** 272011

[32] Wang W, Zou F, Fritzsche S and Li Y 2024 *Phys. Rev. Lett.* **133** 223001

[33] Shabaev V, Glazov D, Ryzhkov A, Brandau C, Plunien G, Quint W, Volchkova A and Zinenko D 2022 *Phys. Rev. Lett.* **128** 043001

[34] Von Der Wense L, Bilous P V, Seiferle B, Stellmer S, Weitenberg J, Thirolf P G, Pálffy A and Kazakov G 2020 *Eur. Phys. J. A* **56** 176